Optics Letters

Real-time *in situ* phase sensitivity calibration of interferometric fiber-optic ultrasonic sensors

Mohammed Alshammari,[1] Yufei Chu,[1,2] (iD) and Ming Han[1,*] (iD)

[1]*Department of Electrical and Computer Engineering, Michigan State University, East Lansing, Michigan 48864, USA*
[2]*Current address: School of Marine and Atmospheric Sciences, Stony Brook University, Stony Brook, New York 11790, USA*
*mhan@egr.msu.edu

Output from a fiber-optic interferometric ultrasonic sensor can be affected by the operating point changes and/or the optical power fluctuations. We report a method for real-time and *in situ* calibration of the responses to ultrasound-induced phase delays for a low-finesse Fabry–Perot (FP) ultrasonic sensor demodulated using a phase-generated carrier. The carrier is produced from an electro-optic phase modulator, and its zero- and fundamental-carrier frequency components yield two quadrature signals. The same phase modulator is employed to generate controllable laser frequency modulations and calibration phase delay modulations. The response to the known calibration phase delays is used to gauge the sensor output in real time and *in situ*. The experiment has verified the effectiveness of the calibration method against the signal variations from both operating point changes and optical power variations.

Fiber-optic interferometric ultrasound sensors [1] have received considerable attention for their applications in structural health monitoring. Ultrasound detection is achieved by detecting the small ultrasound-induced phase changes of the interferometers. An effective implementation of the sensors requires robust and accurate demodulation schemes with good resolution and accuracy. A main challenge comes from the environmental drifts of the sensor spectrum. For edge-filter detection, a method to counter the signal fading and distortion is to lock the wavelength of a laser to the slope of the spectrum where the ultrasound-induced wavelength shift is converted into laser intensity variations [2,3]. However, this scheme is hindered by the limited availability of low-noise laser sources whose wavelength can be continuously tuned with sufficient tuning range and tuning agility. For interferometric sensors with sinusoidal fringes, quadrature demodulation is an effective method for combating the environmental spectral drifts. Quadrature signals can be generated using light sources containing several wavelengths at the quadrature positions of the sinusoidal fringes. This configuration ensures that at least one of the wavelengths is at the sensitive region of the spectral slope regardless of the relative positions of the spectral fringes and

the two wavelengths. The quadrature wavelengths can be generated from a dual-wavelength laser [4], a single laser with fast wavelength switching [5], or a single laser combined with a frequency shifter [6]. Quadrature signals can also be produced using phase-generated carriers (PGCs) with homodyne demodulation [7,8]. The phase delay can be calculated without ambiguity over a large range. These phase demodulation methods are primarily intended for increasing the dynamic range and often have limited resolution for detecting ultrasonic signals. However, the accuracy of the demodulation has often been overlooked. In edge-filter detection, the signal in response to a given ultrasound-induced wavelength shift is affected by both the sign and absolute value of the spectral slope. Optical power changes, which can be from the laser sources, perturbations to the optical path of the sensor system, or the spectral drift of the sensors with non-uniform spectrum can also lead to changes in the optical signal and the consequent measurement errors of the ultrasound. Little attention has been paid to this issue in the past.

Here, we demonstrate a quadrature demodulation scheme with real-time *in situ* calibration of the sensitivity to ultrasound-induced phase delay (or wavelength shift) for an ultrasonic sensor based on a low-finesse fiber-coil Fabry–Perot (FP) interferometer with a relatively long cavity length. The quadrature signals are generated using carriers produced from an electro-optic phase modulator. Real-time *in situ* calibration is achieved by generating a small sinusoidal frequency modulation of the laser source with known modulation amplitude and observing the responses to this modulation, which is used to gauge the sensor response to the ultrasound signal. This scheme does not require a wavelength-tunable laser. Instead, the same phase modulator for generating the carriers is used for the frequency modulation. Therefore, the calibration can be conveniently incorporated into an existing sensor system with little additional cost and complicity.

Figure 1 shows the schematic of the sensor system. The light from a laser passes through a phase modulator and then a circulator before reaching the FP sensor. The phase modulator is driven by a signal combined from two sinusoidal waves of frequencies Ω and Ω_c, where $\Omega \gg \Omega_c$ and Ω_c is also much larger than the maximum frequency of the signal of interest (ultrasound). As explained later, Ω is the carrier that generates the quadrature signals for demodulation and Ω_c is used to generate a laser frequency modulation for real-time *in situ* calibration. The light reflected from the sensor is detected by a photodetector
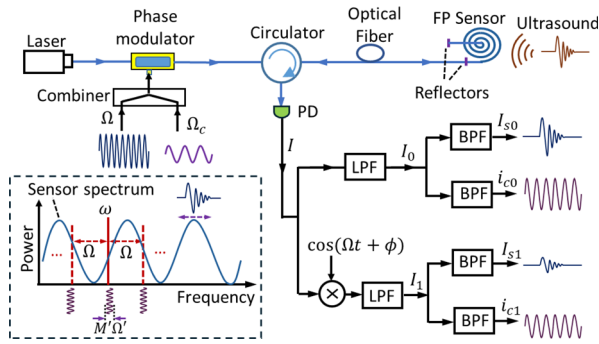
Fig. 1. Schematic of the sensor system with PGC quadrature demodulation and real-time, *in situ* phase sensitivity calibration. PD, photodetector; LPF, low-pass filter; BPF, bandpass filter.

from which the two quadrature signals are extracted. Each signal contains the response to the ultrasound-induced shift of the sensor spectral and the response to the known and controllable frequency modulation of the laser. The latter is then used to calibrate the former to obtain a signal proportional to the ultrasound-induced phase shift.

To establish a quantitative model for the scheme, we first consider the case where wave Ω_c for calibration is absent. In this case, the system reduces to a part of the conventional PGC demodulation method, which has been studied in detail in our previous work [9]. Briefly, the model starts with the complex electrical field of the laser light after the phase modulator:

$$E = E_0 e^{j\omega t + jM \sin \Omega t}, \tag{1}$$

where t denotes time, ω is the optical angular frequency of the laser, and M is the phase modulation depth. Assuming a low-finesse FP sensor, the field reflected from the FP is given by the following:

$$E_r = E_0 \sqrt{R}[e^{j\omega t + jM \sin \Omega t} + T e^{j\omega(t-\tau) + jM \sin \Omega(t-\tau)}], \tag{2}$$

where τ is the time delay caused by the optical propagation of a round trip in the FP and R and T are, respectively, the power reflection and transmission coefficients of the two FP mirrors (assumed identical). The output of the FP, I, is proportional to the power of the reflected light, or $I \propto E_r E_r^*$, where "*" denotes the complex conjugate and is given by the following [9]:

$$I \propto 1 + T^2 +$$
$$2T\left[J_0(C) + 2\sum_{k=1}^{\infty}(-1)^k J_{2k}(C)\cos 2k\Omega\left(t - \frac{\tau}{2}\right)\right]\cos\theta(t) -$$
$$4T\sum_{k=0}^{\infty}(-1)^k J_{2k+1}(C)\cos(2k+1)\Omega\left(t - \frac{\tau}{2}\right)\sin\theta(t), \tag{3}$$

where J_k is the kth-order Bessel function of the first kind, $\theta(t) = \omega\tau$ is the phase delay from the optical propagation of a round trip in the FP, and $C = 2M\sin(\Omega\tau_0/2)$, where τ_0 is the initial round trip time delay (i.e., $\tau = \tau_0 + \Delta\tau$ and $\Delta\tau$ is the change of the time delay caused by the signal of interest as well as by the undesirable environmental perturbations). The validity of Eq. (3) requires the assumptions of $\Omega\Delta\tau \ll 1$ and $\sin(\Omega\tau_0/2) \gg \sin(\Omega\Delta\tau(t)/2)$, which can be fulfilled by selecting the appropriate values of Ω. The output contains a series of components at the carrier frequencies 0, Ω, and 2Ω, as well as

other higher-order harmonics. Here, we obtain the quadrature signals containing $\cos\theta(t)$ and $\sin\theta(t)$ utilizing the carrier frequencies 0 and Ω, respectively. The signal for 0 can be obtained by a low-pass filter (LPF) that removes the other frequency components. The signal for Ω can be obtained by mixing the total output with the carrier frequency Ω followed by a similar LPF. These operations result in the two quadrature signals:

$$\begin{aligned} I_0 &= A + B_0 \cos\theta(t) \\ I_1 &= B_1 \cos\theta(t) \end{aligned}, \tag{4}$$

where A, B_0, and B_1 are constants that are proportional to the optical power. B_0 and B_1 can also be affected by the changes in the fringe visibility of the sensors. We write the phase delay $\theta(t)$ as a sum of two terms $\theta(t) = \tilde{\theta}_0 + \delta\theta_s$, where $\tilde{\theta}_0$ is a quasi-static phase term including the environmental effect and laser wavelength drift and $\delta\theta_s$ is an ac term containing the signal of interest (ultrasound). Assuming the ultrasound-induced phase change is small or $\delta\theta_s \ll 2\pi$, the following approximation: $\sin(\tilde{\theta}_0 + \delta\theta_s) \approx \sin\tilde{\theta}_0 + \cos\tilde{\theta}_0\delta\theta_s$ and $\cos(\tilde{\theta}_0 + \delta\theta_s) \approx \cos\tilde{\theta}_0 - \sin\tilde{\theta}_0\delta\theta_s$ can be used in Eq. (4). Using a bandpass filter (BPF) that matches the bandwidth of the ultrasound, the ac terms containing the ultrasound signal can be obtained:

$$\begin{aligned} i_{s0} &= -B_0 \sin\tilde{\theta}_0 \delta\theta_s \\ i_{s1} &= B_1 \cos\tilde{\theta}_0 \delta\theta_s \end{aligned}. \tag{5}$$

Equation (5) shows that at least one of the quadrature channels will give a sensitive response to the ultrasound signal regardless of the phase delay $\tilde{\theta}_0$. However, the magnitude of the signal $\delta\theta_s$ cannot be accurately determined from i_{s0} and i_{s1}, because they depend on the values of B_0, B_1, and $\tilde{\theta}_0$ that are susceptible to the environmental perturbations.

The calibration scheme allows to retrieve $\delta\theta_s$ and eliminate the uncertainty caused by B_0, B_1, and $\tilde{\theta}_0$. The inset of Fig. 1 shows the conceptual picture of the demodulation and calibration scheme. The phase modulation of the laser at appropriate carrier frequency Ω generates multiple lines. The beating of the laser lines produces the frequency components in Eq. (3), which leads to the two quadrature signals in Eq. (4). Ultrasound causes small changes in the round trip time delay of the light in the FP, reflected by the frequency shifts of the FP spectrum, leading to the responses in Eq. (5). To calibrate the responses, the frequency of the laser is modulated with a small and controllable amplitude at frequency Ω_c. The frequency modulation of the laser is equivalent to producing a known phase delay modulation, which leads to proportional responses with the same coefficients in Eq. (5). Therefore, the responses to the known phase changes from the laser frequency modulation can be used to gauge the responses to ultrasound-induced phase changes, yielding a measurement independent on B_0, B_1, and $\tilde{\theta}_0$.

The frequency modulation for calibration can be achieved by the same phase modulator used to produce the carrier. The light from the laser after the phase modulator with the modulation signal Ω_c is given by $E_0 = \exp(j\omega t + jM_c \sin\Omega_c t)$, where M_c is the modulation depth associated with the calibration modulation signal. When $M_c\Omega_c$ is small, the laser can be considered as having a time-varying frequency and the instantaneous value of the laser frequency is given by $\omega(t) = \omega + M_c\Omega_c\cos\Omega_c t$. Since the phase delay of the FP is given by $\theta(t) = \omega\tau$, this laser frequency delay modulation corresponds to an FP phase delay modulation of $\delta\theta_c\cos\Omega_c t$, where $\delta\theta_c = M_c\Omega_c\tau_0$ is the modulation amplitude. Because M_c, Ω_c, and τ_0 are all known and unaffected by the optical power or the environment, $\delta\theta_c$ is a constant independent on
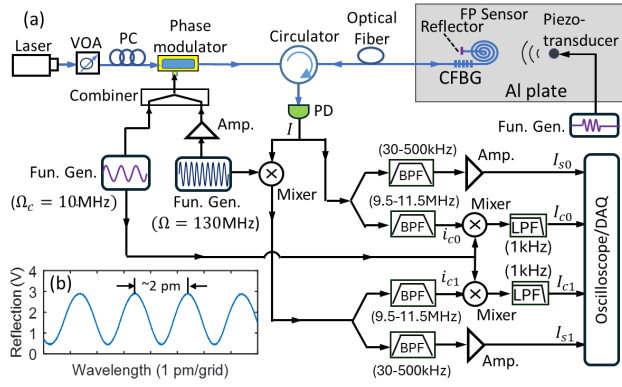
Fig. 2. (a) Schematic of the experimental setup. (b) Spectral fringes of the sensor reflection.

Fig. 3. (a) and (b) Recorded ultrasonic signals and calibration signals as the laser wavelength was scanned. (c) and (e) Ultrasonic signals in detail at different operating points and the corresponding signals after calibration (d) and (f).

optical power and environmental perturbations. The calibration signals from the quadrature demodulation are sinusoidal, i.e., $i_{c0}(t) = I_{c0}\cos\Omega_c t$ and $i_{c1}(t) = I_{c1}\cos\Omega_c t$, and the amplitudes, I_{c0} and I_{c1}, take a form similar to Eq. (5):

$$\begin{aligned} I_{c0} &= -GB_0\sin\tilde{\theta}_0\delta\theta_c \\ I_{c1} &= HB_1\cos\tilde{\theta}_0\delta\theta_c \end{aligned}, \qquad \textbf{(6)}$$

where G and H are two constants accounting for the differences in the electronics (filters and amplifiers) for obtaining the ultrasound-induced signal and the amplitude of the calibration signal. Note that G and H do not depend on the operating points and optical power. Using Eqs. (5) and (6), we can obtain the calibrated ultrasound-induced phase delay:

$$\begin{aligned} \delta\theta_s &= (Gi_{s0}/I_{c0})\delta\theta_c \\ \delta\theta_s &= (Hi_{s1}/I_{c1})\delta\theta_c \end{aligned}. \qquad \textbf{(7)}$$

In theory, the two expressions in Eq. (7) give the same results for $\delta\theta_s$; in practice, the one with a larger $\delta\theta_c$ that gives a higher signal-to-noise ratio (SNR) should be used. As the laser frequency modulation and its responses are obtained in real time during the sensor operation, the calibration is real time and *in situ*.

The experimental setup to demonstrate the calibration and the demodulation schemes is shown in Fig. 2(a). The FP sensor was made from a bend-insensitive fiber. One of the reflectors for the FP is a chirped FBG and the other was a metal film. The fiber between the two reflectors was ~40 cm long and was made into planar circular coils with an inner diameter of 6 mm and an outer diameter of 8 mm. During fabrication, the bending-induced birefringence of the fiber was controlled to yield a sensor insensitive to the polarization of the probe light [8]. The coil was placed on the surface of an aluminum plate to detect the identical, repetitive ultrasonic pulses generated from a piezo transducer with a repetition rate of 40 Hz. Figure 2(b) is the reflection spectrum of the FP sensor measured with a wavelength-scanning laser along with a photodetector, showing a free-spectral range (FSR) of ~2 pm.

We used a wavelength-tunable external-cavity laser combined with a variable optical attenuator (VOA) as the light source, which allows us to change the operating points and the optical power for testing the demodulation and calibration scheme. The light polarization was controlled using a polarization controller (PC) to maximize the modulation efficiency of the phase modulator. The phase modulator was driven by a combined signal
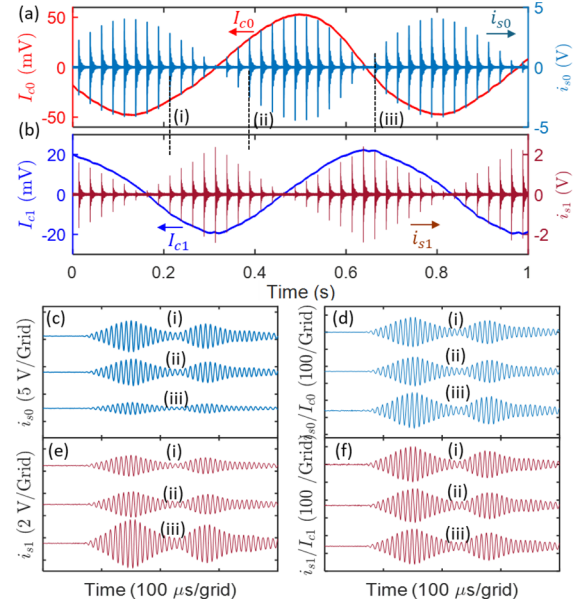
of two sinusoidal waveforms of frequencies $\Omega/2\pi = 130\,\text{MHz}$ (carrier for quadrature demodulation) and $\Omega_c/2\pi = 10\,\text{MHz}$ (for calibration) from two function generators. After passing through a circulator, the light reached the sensor, and the reflected light was directed to an amplified photodetector with a bandwidth of 25 kHz–125 MHz. The zero-carrier frequency component has the cosine term. The ultrasound-induced signal (i_{s0}) and the calibration signal (i_{c0}) were filtered out directly from the PD output with bandpass filters of appropriate bandwidths. The signals (i_{s1} and i_{c1}) in the sine term were obtained by mixing the PD output with sinusoidal waves at the fundamental-carrier frequency (Ω) followed by bandpass filters of appropriate bandwidths. The ultrasound-induced signals were further amplified with a gain of ~40 dB to increase the SNR. The calibration signals (i_{c0} and i_{c1}) were sinusoidal waveforms at Ω_c. Only their amplitudes (I_{c0} and I_{c1}) were needed for calibration, which were obtained by mixing i_{c0} and i_{c1} with sinusoidal waveforms at the modulation frequency Ω_c.

We tested the effectiveness of the calibration scheme for signal variations caused by operating point changes. The laser wavelength was scanned over a range of several FSR of the sensor (the laser power remained constant), which is equivalent to varying the quasi-dc phase term, $\tilde{\theta}_0$, over several cycles, and the two ultrasound-induced signals, i_{s0} and i_{s1}, and the calibration signals, I_{c0} and I_{c1}, were continuously recorded using a data acquisition (DAQ) device with a sampling rate of 2 MS/s. The results are shown in Fig. 3(a) for i_{s0} and I_{c0} and in Fig. 3(b) for i_{s1} and I_{c1}. The amplitudes of the ultrasound signals fluctuated significantly with varying laser wavelength and vanished at several points. However, at least one of the ultrasound signal channels gave a sensitive response to the ultrasound regardless of the phase $\tilde{\theta}_0$. The calibration signals followed the envelopes of the corresponding ultrasound signals closely, indicating that the calibration signal can be used to effectively gauge the ultrasound signals. Ultrasound signals (i_{s1}) obtained using the zero-carrier frequency at three different operating points
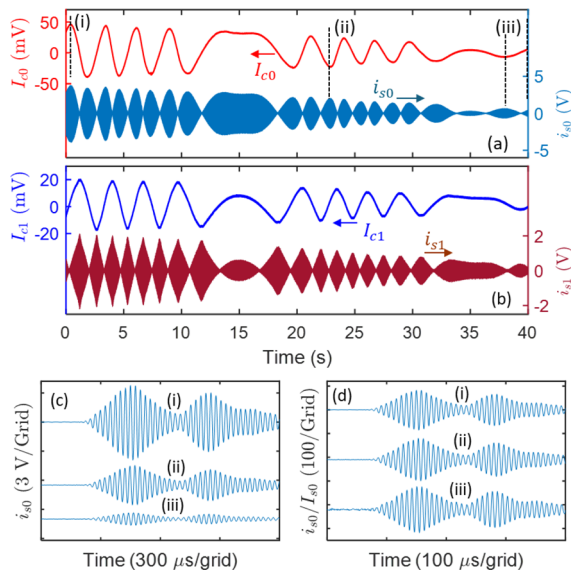
Fig. 4. (a) and (b) Recorded ultrasonic signals and calibration signals as the laser wavelength was scanned and the laser power was reduced. Ultrasonic signals in detail before (c) and after (d) calibration.

indicated in Fig. 3(a) are shown in more detail in Fig. 3(c). Their amplitudes have large variations. The results after calibration using Eq. (7) are shown in Fig. 3(d) with much more consistent amplitudes. The corresponding ultrasound signals obtained using the fundamental-carrier frequency before and after calibration are shown in Figs. 3(e) and 3(f), respectively. Again, the calibration yields much more consistent amplitudes of the ultrasound signal. These results verify that the calibration scheme is effective against the drift of operating points and can be performed in real time and *in situ*. Specifically, Figs. 3(c) and 3(d) show that, without calibration, the ultrasound signal (i_{s0}) at (ii) is 15% lower than at (i), and the difference of the same signals after calibration (i_{s0}/I_{c0}) is reduced to <1%. The calibration at (iii) is less accurate because the signal is small. In practice, this signal would be discarded and i_{s1}/I_{c1} in Fig. 3(f) that leads to much more consistent results would be used.

Then we test the effectiveness of the calibration method against optical power variations (along with operating point drifts). The laser wavelength was scanned to continuously change the operating points. In the meantime, the optical power injected into the sensor was reduced by manually adjusting the VOA. During the process, the ultrasound signals, i_{s0} and i_{s1}, and the calibration signals, I_{c0} and I_{c1}, were continuously recorded using the DAQ. The time evolutions of the signals are shown in Fig. 4(a) for I_{c0} and i_{s0} and in Fig. 4(b) for I_{c1} and i_{s1}. Because the optical power changes were slow compared with the operating point changes from laser wavelength scanning, the envelopes of the ultrasound signals and the calibration signals are proportional to the optical power. Figures 4(a) and 4(b) show that the changes in the optical power indicated by the envelopes of the two ultrasound signals (i_{s0} and i_{s1}) are consistent, which are also consistent with the envelopes of their corresponding calibration signals (I_{c0} and I_{c1}). From the envelopes, the optical power was reduced by more than 6 dB during the process. Figures 4(c) shows the detected ultrasound signals obtained using the zero-

carrier frequency at three different optical power levels marked in Fig. 4(a). An operating point yielding a maximum response was selected at each optical power level to clearly show the changes in the optical power. The detected signals show large variations in their amplitude. The signals were calibrated using Eq. (7) and the results are shown in Fig. 4(d). All three waveforms have approximately equal amplitudes, which verify the effectiveness of the real-time *in situ* calibration method against optical power variations.

The sensor response was calibrated against the FP phase delay. In practice, the sensor needs to be calibrated against ultrasound, which can be done by exposing the sensors to a known ultrasound field and comparing the ultrasound signal, the calibration signal, and the known ultrasound field. The phase delay modulation for calibration generated from the phase modulator is expected to be stable over long periods. In practice, the long-term stability of ultrasound calibration is likely determined by the stability of the coupling mechanism between the structure and the sensor.

In summary, we demonstrated a method for real-time and *in situ* calibration of the responses to ultrasound-induced phase delays of a fiber-optic interferometric ultrasonic sensor. The sensor was a low-finesse FP interferometer with a relatively long cavity length that allows the use of an electro-optic phase modulator to generate the carrier for PGC quadrature demodulation using the zero- and fundamental-carrier frequency components. The same phase modulator was employed to produce sinusoidal calibration phase delays with a constant amplitude at a frequency much larger than the ultrasound frequency. The responses to the calibration phase delays were extracted and used to gauge the response to ultrasound in real time and *in situ*. Experiments were performed and validated the effectiveness of the calibration method against the signal variation from both operating point changes and optical power fluctuations. Because of the large bandwidth of the electro-optic phase modulator, the bandwidth of the sensor system with calibration is limited by the sensor head itself. The demodulation method and calibration scheme demonstrated here are also applicable to sensors based on other types of two-beam interferometers such as Michelson interferometers and Mach–Zehnder interferometers.

REFERENCES

1. R. Soman, J. Wee, and K. Peters, Sensors **21**, 7345 (2021).
2. A. Li, Z. Jing, Y. Liu, *et al.*, IEEE Sens. J. **21**, 2084 (2021).
3. X. Mao, S. Yuan, P. Zheng, *et al.*, J. Lightwave Technol. **35**, 2311 (2017).
4. A. Pinto, O. Frazão, J. Santos, *et al.*, J. Lightwave Technol. **28**, 3149 (2010).
5. Q. Liu, A. Li, Y. Liu, *et al.*, J. Lightwave Technol. **39**, 3991 (2021).
6. G. Liu, Y. Zhu, Z. Liu, *et al.*, Opt. Lett. **44**, 2756 (2019).
7. A. Dandridge, A. B. Tveten, and T. G. Giallorenzi, IEEE Trans. Microwave Theory Tech. **30**, 1635 (1982).
8. G. Liu, Y. Zhu, Q. Sheng, *et al.*, Opt. Lett. **45**, 4164 (2020).
9. F. Karim and M. Han, Opt. Express **31**, 9769 (2023).